Isotope Separation On-Line at ISAC

Olivier Shelbaya

November 7, 2016

Abstract

This is an overview of the ISAC Mass Separator (IMS) system at TRIUMF, its operating principles, and some of the underlying physics. It is a resource intended to provide a convenient collection of information, citing relevant articles and publications, should the reader want to deepen his or her knowledge of the topics presented. Not all are covered with the same degree of depth. The nuclear physics overview is purposely covered at a more qualitative level, given the ease with which such a topic can become highly technical, and given the objective of this document. The emittance section is covered with more detail, as it is a frequent topic of discussion in the process of low energy tuning. The rest focuses on the more practical aspects of the IMS system itself, and its principle of operation.

Isotope Separation On-Line at TRIUMF

The production of isotopes driven by charged particle bombardment of a target material is referred to as on-line production. This technique makes possible the production of short-lived radionuclei, however it is interdependent with the ability to precisely separate isotopes by mass. In general, the mass (or isotope) separation is accomplished using mass spectrometry via one or several bending magnets whose fields are fine-tuned to allow transmission of a specific mass to charge ratio (also referred to as m/q).

500MeV protons from the TRIUMF cyclotron are used to induce nuclear reactions within a target material held at high voltage (HV). The products are ionized while exiting the target and are extracted into the ISAC (Isotope Separator and ACcelerator) Mass Separator (IMS) system. The IMS beamline section is used to select a particular m/q, and to fine-tune the beam properties prior to delivery to the rest of the ISAC facility.

ISAC Targets and Nuclear Reactions

Targets at ISAC are divided into two basic classes, low and high power (LP/HP), referencing their ability to sustain and effectively dissipate heat generated by interaction with 500MeV proton current. Targets are designed such that the incident proton beam deposits approximately 90% of its energy within the target material, the rest being absorbed by a beam dump downstream [1]. Low power targets can dissipate 4-5kW, while high power targets dissipate > 25kW[4]. Practically, this corresponds to p+ currents up to 50uA for LP and up to 100uA for HP.

Targets are heated by both the incident proton beam, and by a series of heater coils operating at up to 600A. Target temperature at ISAC is constrained to produce a vapor pressure not exceeding 10^{-6}mbar. Generally, this translates to central target temperatures between 1600-2200°C. Operation at higher target temperatures would cause target material evaporation, decreasing output efficiency.

Material Type	Elements
Refractory Metals	Ti, Zr, Nb, Ta
Lanthanides	Th, U
Other	Si, Ni

Table 1: Target materials used at TRIUMF-ISAC (2016).

With the heaters on, the target maintains temperature equilibrium by blackbody emission. Target temperatures are calculated by considering the Stefan-Boltzmann blackbody radiation law [2]:

$$E = \epsilon \sigma A(T^4 - T_0^4) \tag{1}$$

where ϵ is the target emissivity, σ the Stefan-Boltzmann constant and A is the target heat emitting surface area. Equation 1 provides a base framework with which target foil temperatures can be predicted, prior to the additional heating effects of 500MeV protons. With this baseline temperature model, the proton heating effect can be computed using numerical simulation methods, such as SRIM[1] [3]. Targets simulated in SRIM are used to compute dE/dx for various proton currents, producing a series of heater curves which are provided to ISAC operations, detailing the target heating in terms of heater currents versus temperture. These are shown in Figure 3. Note how the high power target on the right in Figure 3 has a much flatter heating curve than the low power (left), a product of its enhanced ability to dissipate heat.

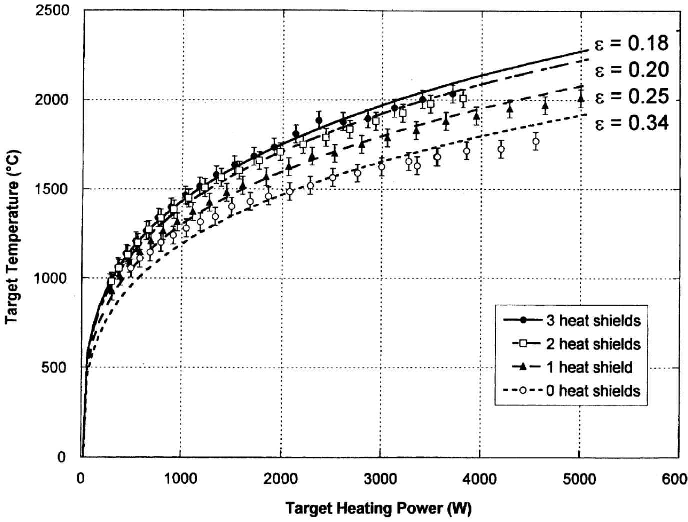

Figure 1: Blackbody heating curves for ISAC targets with various heat shield configurations.

Target materials used at ISAC can generally be divided into two categories, shown in Table 1: refractory metals (20<A<100) and lanthanides (A>200). Silicon and niobium are also used for lighter isotope production. The target holder, a 19cm long by 20mm diameter Ta tube, holds together a series of thin foils (< 0.2mm), consisting of the desired material. This is shown in Figure 2. For metals such as Nb & Ta, pure elemental foils can be used, while for the other materials of Table 1, elemental ceramic compounds (such as SiC, TiC, ZrC, etc..) are chemically bound with solvents to thin exfoliated graphite foils using organic binders and plasticizers [4]. This generally produces ceramic layers of 0.25mm on the foils. The foils are then loaded into the target container tube and heated to induce the breakdown and evaporation of the various chemicals used in the aformentioned process.

---

[1] SRIM - the stopping and range of ions in matter - is a simulation package which computes the interactions between charged energetic particles in matter.

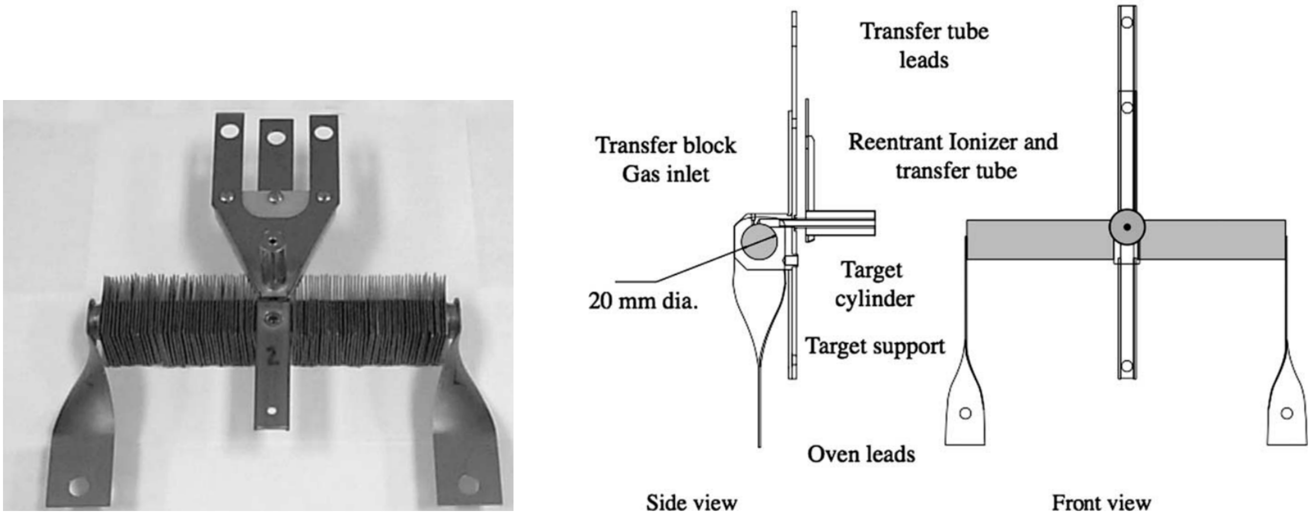

Figure 2: L: Photograph of a high power ISAC target holding tube with exterior tantalum fins used as heat sinks. R: Diagram of an ISAC target showing both side and front view. Note that on the front view, the ionizer tube is facing outside of the page. The flat metal leads are the tube (straight) and target (twisted) heater connectors, respectively.

At the midpoint of the target housing, a perpendicularly oriented Ta transfer tube serves as a guide between the target volume and the ion source. Within the Ta guide, a rhenium foil acts as a surface ionizer for the isotopes in transit. Beyond the ionizer lie the target extraction optics including the extraction electrode (EE), held at a few hundred volts above the target bias, which helps to define an outward streaming of ions from the ionizer, matching the beam profile to the optics downstream. The geometric configuration and relative biasing of the various electrodes that define the ion source are optimized by ion optics simulation, and aim to produce a collimated ion beam which can be transported to the rest of the IMS section.

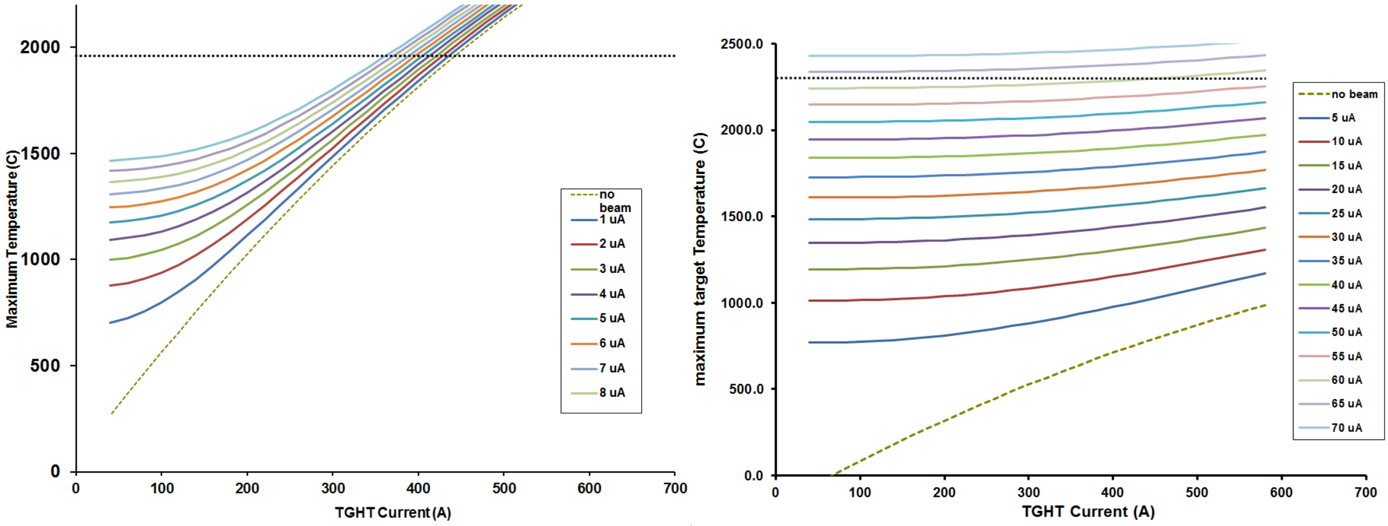

Figure 3: L: Heater curves for a low power (LP) UCx target. R: Heater curves for a high power (HP) Ta target. The horizontal dotted black line represents the desired operating temperature.

The harsh radiation environment in which the target operates places a limit on its useful lifetime. While nuclear chemistry does take place within the foil materials affecting isotope yields over time, physical target degradation also takes place. An example is the condensation of radiogenically-produced isotopes on the EE producing asymmetric electric fields, potentially affecting the output ion beam quality[1]. ISAC targets generally have a lifetime on the order of 3-4 weeks after which, reliable operation and output cannot be guaranteed.

To better understand the output of different target foil materials, a brief overview of the three main nuclear reactions [1] which govern the interaction with 500MeV protons follow:

Nuclear Spallation

A spallation reaction at the nuclear level involves an incident particle collision causing the ejection of several nucleons from the target nucleus. It is a two step set of nuclear reactions [8]. The first step involves collisional energy transfer, raising the nucleus to an excited state. Also during this phase, it is possible for energetic (>20MeV) particle emission from the nucleus including neutrons, protons and pions. Conservation of momentum dictates that these emissions will be in roughly the same direction as the incident projectile. Secondary emitted particles can induce further spallation reactions in adjacent nuclei.

The second step involves the de-excitation of the nucleus. Since protons experience a stronger binding caused by the Coulomb barrier within the nucleus, neutron emission is energetically favored. Several low-energy (<20MeV) neutrons are emitted from the core, a process known as neutron evaporation. The evaporation reaction can also eject protons and alpha particles, albeit to a lesser degree of probability. Spallation reactions of heavy elements such as uranium favor production of neutron rich isotopes with a slightly lesser mass than that of the target material. This can be understood by the fact that the ejection of protons, even though less likely, still occurs at an appreciable rate. ^{238}U, itself possessing 92 protons and 146 neutrons, can lose dozens of neutrons and remain neutron rich.

Nuclear Fragmentation

Similar to the case of spallation, this process begins with an energetic particle interacting with an atomic nucleus, and the reaction can also be thought of as a two step process [9]. The first step is much the same as for spallation, and resulting in energy deposition within the nuclear core and possible energetic particle emission. However, unlike spallation, the excited nucleus sheds its energy by splitting up into metastable fragments, in addition to the ejection of several neutrons. This process generates a distribution of fragment masses. A specific example of this is U producing Na and Pb. As heavier nuclei tend to carry an excess of neutrons, the fragments have a tendency to keep a statistical memory of the neutron-proton ratio. In other words, the fragmentation of a neutron-rich nucleus is likely to produce neutron rich nuclei in turn.

Induced Fission

A precondition for fission is that the target material be fissile. While all nuclei are fissionable, i.e., it is possible to cause fission by particle bombardment at sufficiently high energies, for the nucleus to be considered fissile the cross section (probability) of fission has to be of high probability for collisions with thermal neutrons. The latter possess a kinetic energy of ~ 0.025eV. The probability of fission will then be of comparable order to processes such as spallation or fragmentation. Only heavy elements for $Z > 90$ meet this criterion. At ISAC, this corresponds to Thorium and Uranium targets only. The induction of fission produces a broad distribution of daughter nuclei, again favoring a statistical memory of the parent neutron excess. The typical fission product mass ratio is around 3:2.

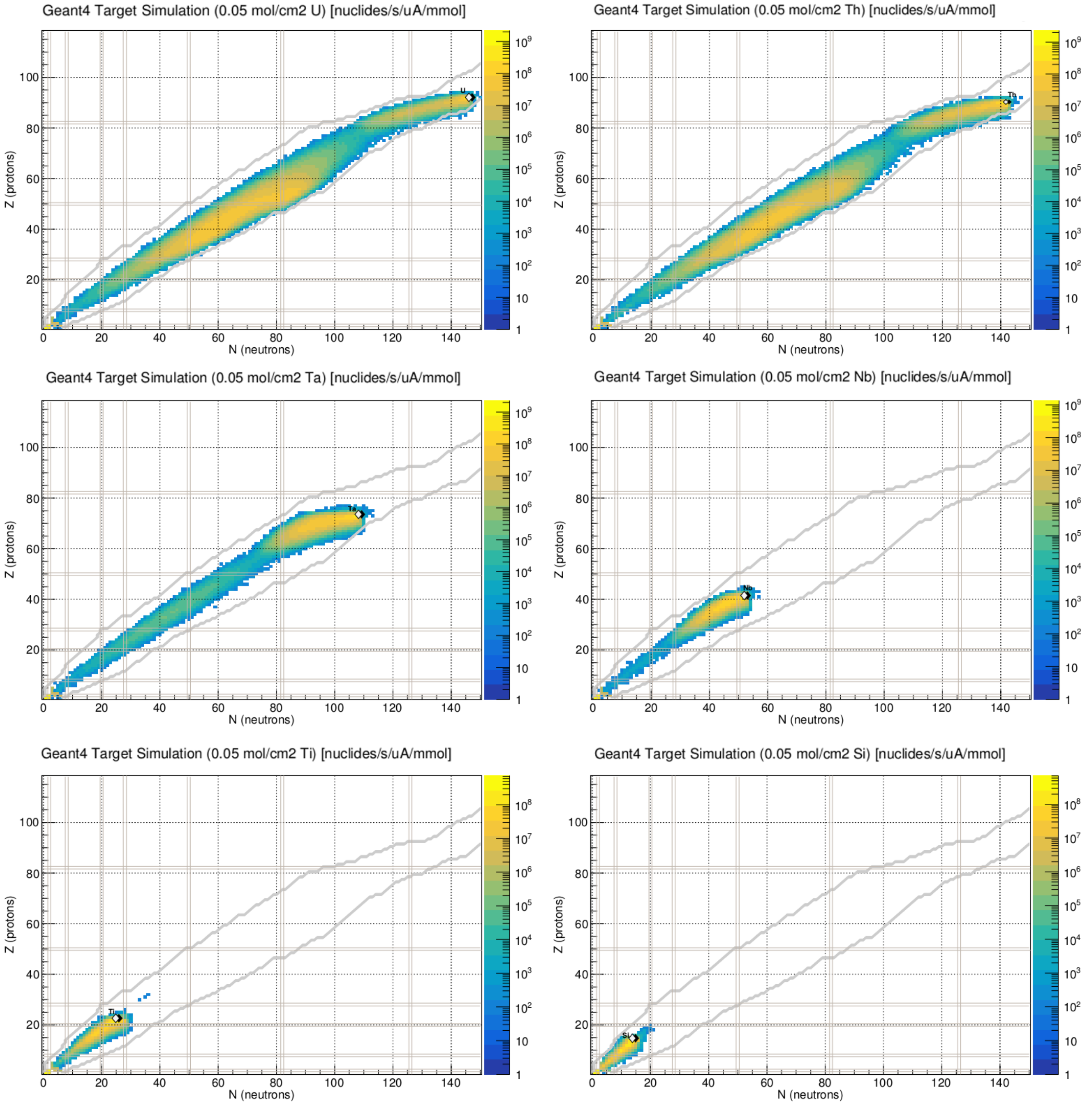

Figure 4: Simulated radioactive isotope yields at ISAC with indicated target materials (2016). Heat map indicates yields in ions/second. The yield charts were generated using GEANT4, a simulation package for the passage of particles through matter, based on the ISAC target geometry. Produced by and used with permission from Peter Kunz.

Yields and Target Chemistry

Each of the aformentioned mechanisms, simultaneously at play, will then produce radioactive isotopes at different mass regions relative to the target nuclei. Spallation products will peak a few mass units below the target, while fragmentation and fission will populate a broader distribution of masses that reach down to the low mass region. The choice of target material determines the overall mass distribution of generated radioactive isotopes. Since all three processes at play involve the breakup or degradation of a nucleus, an overwhelming number of products will be of lower mass than that of the target material. Given the extremely large quantity of reactions taking place within the target, some much less probable processes such as fusion cannot be entirely discounted; however, these will have an extremely low rate of production. The former can produce isotopes of heavier mass than the target material. Figure 4 shows the simulated radioactive ion beam (RIB) yields generated from all targets shown in Table 1, while Figure 5 shows the cumulative yields that have been measured at ISAC to date.

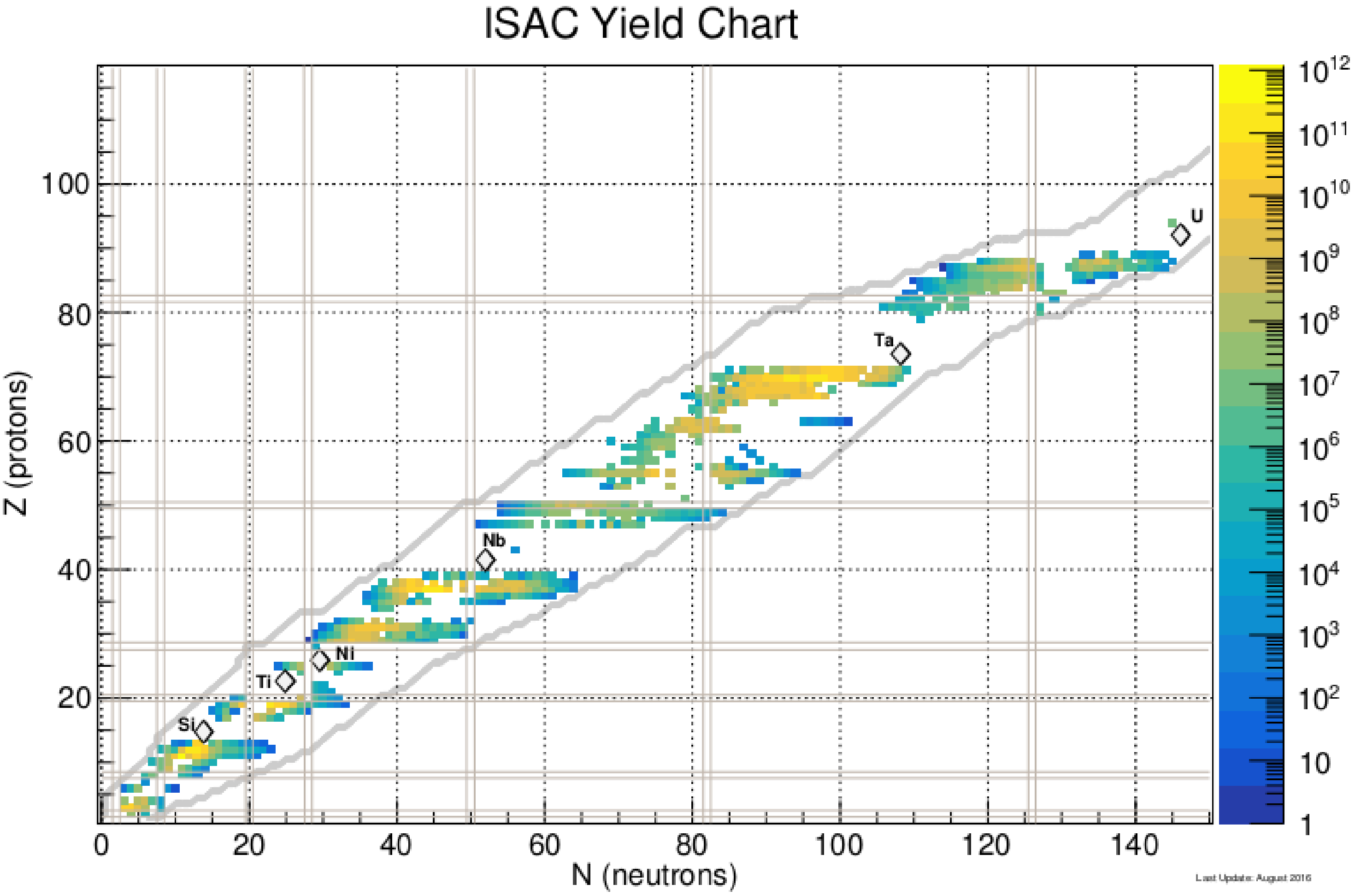

Figure 5: Radioactive isotope yields measured at ISAC with various target materials as of August 2016. Heat map indicates yields in ions/second. Produced by and used with permission from Peter Kunz.

After a given bombardment time t, the instantaneous total population of radioactive reaction products within the target asymptotes toward an equilibrium population N_0, consisting of all generated reaction products:

$$N_0 = \frac{\sigma N_t \Phi_p (1 - e^{-\lambda t})}{\lambda} \tag{2}$$

where λ is the decay constant, σ the proton-target reaction cross section, Φ_p the proton flux and N_t the available target atom population. If at any time proton bombardment ceases, the total radioisotope population immediately decays following:

$$N = N_0 e^{-\lambda t} \tag{3}$$

Of course, radioactive decay takes place constantly, including during extraction from the target and transport to experiments. The total yield at an experiment downstream is then a function of the efficiency of the various steps involved in production and transport:

$$Y = \sigma N_t \Phi_p \epsilon_r \epsilon_i \epsilon_a \epsilon_d \tag{4}$$

the factors ϵ_i are, in sequence, the release, ionization, acceleration and decay efficiencies, all of which are ≤ 1. The release and ionization efficiencies are inherent to the target design and operation parameters (temperature, material, electric fields, etc..). Acceleration efficiency in the case of the IMS section is tune-dependent and thus directly controllable by operators. As for the decay efficiency, it obviously depends on the amount of time between production and experiment delivery. As an example, a beam of ^{26}Na ($t_{\frac{1}{2}} = 1.07$ s) at 28kV source bias will travel at a velocity of ∼4.5x10^5 m/s. For an experiment 100m away from the source, this corresponds to a flight time of roughly 220 microseconds. Considering that it takes 7 half lives for a population to decay below 1%, the number of isotopes that successfully reach the experiment is >99%. Prior to target extraction however, the time taken for radioisotopes to find their way from within the target material to the ionizer tube is another important factor in the decay efficiency. To better understand this, it is necessary to consider the physics of ion transport within the target material.

At the atomic level, the target material (TiC, ZrC, etc..) is arranged in a regular lattice structure. Interaction with the proton beam produces radioisotopes within the lattice, thanks to the three main nuclear reactions described above. High lattice temperatures induced by both proton beam and target heating permit the diffusion of isotopes within the crystalline structure. Diffusion in a solid can be characterized by the Arrhenius equation:

$$D = D_0 e^{(-E_a/kT)} \left[\frac{cm^2}{s}\right] \tag{5}$$

D_0 is an isotope-specific constant, E_a is the atomic activation energy required to move an atom within the lattice from site to site [5], k is Boltzmann's constant and T is the target temperature. The units of diffusion are presented as area per unit time. Eq. 5 shows that the rate of diffusion increases with temperature, meaning a uniformly heated target will result in a more rapid diffusion of isotopes, reducing decay inefficiencies. Once isotopes reach the material boundary, they can undergo effusion from the target material. The released, gaseous radioisotopes then effuse toward the transport tube-ionizer. The effusion process can be characterized by its average container exit time, t_x:

$$t_x = \frac{1}{\Gamma_x} = \frac{1}{\bar{v}}\frac{4V}{A_x} = \sqrt{\frac{\pi m}{8kT}}\frac{4V}{A_x}[s] \tag{6}$$

The constant Γ_x is the rate of gaseous collisions per unit area within the target container with volume V and exit area A_x, $\bar{v}$ being the average molecular velocity. The average exit time of Eq. 6 inversely depends on temperature, again meaning that higher target temperatures lower the exit time, decreasing radioactive losses. Eq. 6 also infers that a target container with a smaller volume and a large exit area will favor shorter effusion times. Each collision with the target vessel carries with it a nonzero molecular adhesion time due to the process of adsorption in which atoms at the material interface interact. This causes an increase of the effusion exit time of Eq. 6 by introducing an adsorption sticking time, expressed with the Frenkel equation:

$$\tau = \tau_0 e^{(\Delta H/kT)}[s] \tag{7}$$

where $\tau_0 \sim 10^{-13}$ s is the lattice vibration period and ΔH is the chemistry-dependent adsorption enthalpy specific to each adsorbed atom on the target container surface. The adsorption delay decreases with increasing temperature. Summarizing the effects of Eqs. 5, 6 an 7, operating a target at high temperature dereases the time between radioisotope production (spallation, fragmentation, fission) and target extraction by:

- decreasing the time taken by radioisotopes to exit the target material (diffusion)
- decreasing the time taken by gaseous radiosotopes to find their way to the ionizer tube (effusion)
- decreasing the molecular adhesion time for each collision with the inner target container (adsorption)

Some of the gaseous atoms entering the ionizer tube then interact with its metallic surface and are ionized. The fraction α of ions to atoms leaving a surface after interaction can be described by the Saha-Langmuir equation:

$$\alpha = \frac{g_i}{g_a} e^{(\Phi - I_p)/kT} \tag{8}$$

where I_p is the ionization potential, Φ is the minimum energy required to eject an electron from a surface into a vacuum, g_i & g_e are the available ionic and atomic electronic states (degeneracy). Following this, the atomic ionization efficiency β is:

$$\beta = \frac{\alpha}{1 + \alpha} \tag{9}$$

Calculated ionization efficiencies on a tantalum ionizer versus temperature are shown in Figure 6, for several elements [6]. Considering the aformentioned target outgassing pressure constraint 10^{-6}mbar, inspection of Figure 6 suggests operating targets in the vicinity of 2000K produces an acceptably optimized ionization coefficient for several atomic species.

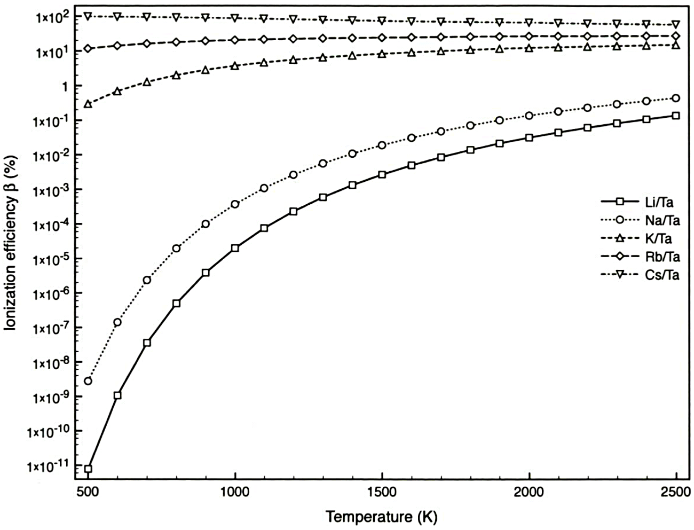

Figure 6: Ionization efficiency β in percentage on a tantalum ionizer for several listed atoms versus temperature. Plot taken from [6].

Intense proton irradiation not only heats the target but also induces a phenomenon known as Radiation Enhanced Diffusion (RED), a process in which energetic protons eject atoms from their position in the lattice leaving behind unoccupied vacancies. The highly mobile populations of both free atoms and lattice vacancies, known as Frenkel pairs, permit the enhanced diffusion of radioisotopes from the target material given their subpicosecond lifetimes [7]. This effect enhances the diffusion of radioisotopes (Eq. 5) from within the material and is particularly advantageous for the transport of short-lived isotopes. RED is proportional to proton flux Φ_p, producing a yield which is nonlinearly proportional to between Φ_p and Φ_p^2, depending on various material properties.

On the other hand, the large scale production of virtually all lower-than-target mass nuclides (see Figure 4) combined with the effects of RED favors the production of various stable compounds within the target material, which can disrupt both the integrity and thermal conductivity, possibly leading to target overheating. This places an upper limit on the useful operating lifetime of a target, which is generally on the order of a few weeks. An example of the above described effects was found on ISAC target Ta#35 HP, with 16.6g Ta/cm^2, after operation for 57723 μA·Hr, receiving 1.1x10^{21} protons. Post-run analysis found that an estimated 41mg of the tantalum target material had been transmuted to impurities after undergoing various nuclear reactions. ISAC targets, metal foil ones in particular, are known to exhibit decreased yields towards the end of their running time due to the above. It is speculated in [4] that composite carbide targets are less susceptible to aging effects because of their porous nature, effectively increasing the surface area available for diffusion.

Isotope Separation

The above mechanisms allow the generation of a broad range of isotopes across different mass regions and lifetimes. Successful delivery requires the isolation of specific masses from the initial target output beam, which can be challenging when considering that isobaric[2] sequences are simultaneously produced. For two isobars, the mass difference is due to both the proton-neutron mass difference (about 0.1%) and the variation in binding energy per nucleon for each species. This can result in mass differences well below 0.01% total isotope mass. For most targets, there is no controllable suppression mechanism and all isotopes are simultaneously extracted[3].

Mass spectroscopy is employed to achieve separation of isotopes, post-production. The radius of curvature of a charged particle, accelerated by an extraction voltage V_e is defined by:

$$r_i = \frac{1}{B}\sqrt{\frac{2m_i V_e}{q}}. \tag{10}$$

If we consider the case of two isobars of roughly the same mass m, source-extracted at voltages of V and V':

$$\frac{r'}{r} \approx \sqrt{\frac{V'}{V}} \tag{11}$$

it is apparent that a higher extraction voltage will produce a higher degree of separation. The mass separator magnet is located on an isolated platform, which can be biased up to 60kV, to supplement the source/target extraction voltage and increase the mass resolution if needed[4].

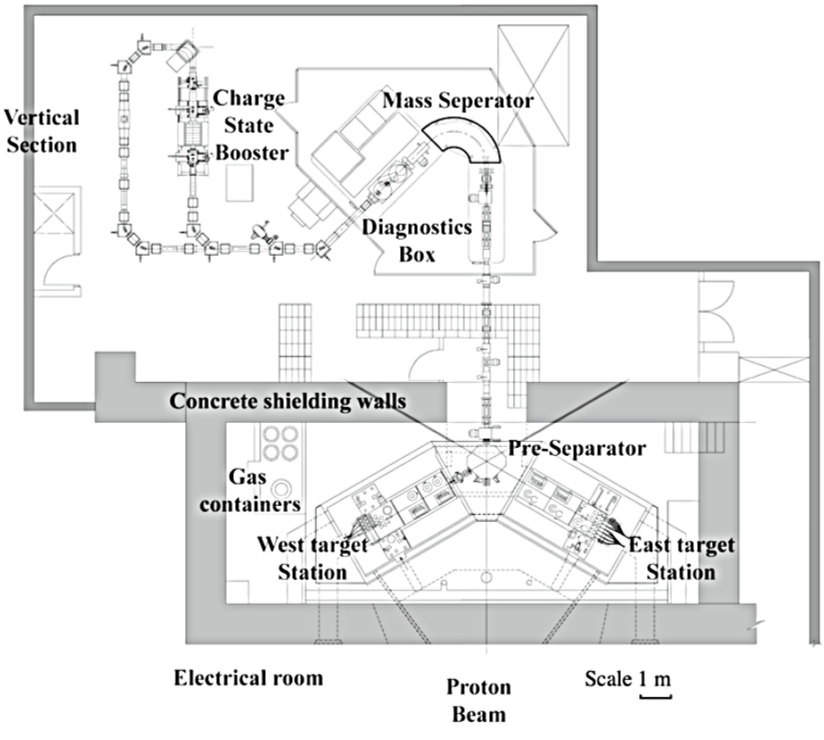

Figure 7: The ISAC Mass Separator (IMS) beamline section.

---

[2] isotopes with the same total number of protons + neutrons

[3] laser ionization sources are an exception to this, as the ionization potential for a particular species can be selected.

[4] as of 2016, this feature has been tested but not used for production as both the extraction voltage and user requirements have not demanded it.

In the IMS section (shown in Figure 7), isotope separation is achieved with two successive separator magnets capable of handling extraction voltages from 12 to 60kV [10]. The first spectrometer, a ±60° hexagonal magnet (to accomodate either target station), functions as a pre-separator achieving a coarse mass selection of $M/\Delta M$ on the order of 100. This is generally good enough to pick out a few isobars, removing all other masses. This also limits the propagation of unwanted radioactive isotopes further in the IMS section, preventing higher contamination of the devices beyond. The pre-separator is designed to act as a shield against this contamination. The pre-separator is also equipped with optical viewports to accomodate laser ionized targets.

High resolution mass separation is then accomplished thanks to a 135° bending magnet, complete with field-correction coils. The separator magnet, originally acquired from Chalk River Laboratories, can achieve a mass resolution of $M/\Delta M = 2000$. While this is generally sufficient to eliminate isobaric contamination, there are notable exceptions such as the rubidium-strontium families for which many isobars are unresolvable ($M/\Delta M > 2000$). After transition through the mass separator, the dispersion of the various masses is of roughly 2m (Eq. 10), meaning most unwanted isobars will be deposited in the beamline housing itself.

Procedurally, given the extremely precise mass selection that may be required, a pilot beam of known mass and generally stable (such as ^{238}U for a UCx target) is used for initial setup of the separator magnets. Pilot beam intensities typically exceed that of radioactive isotopes by several orders of magnitude. Once tuned, the magnetic fields are scaled from m_1 to m_2 following Eq. 10:

$$\boxed{\frac{B_2}{B_1} = \sqrt{\frac{m_2}{m_1}}} \tag{12}$$

The above represents the basic method in which isotopes can be selected with precision, requiring the availability of known pilot isotopes. Each target has at least one of such pilots, if not more. A further consideration, given the imperfect nature of power supplies and current regulation, is that in practice Eq. 12 is more accurate for smaller differences in B_1, B_2. For instance, scaling from ^{238}U to ^{8}Li will generally produce an off-peak scale, which will have to be manually optimized. Thus, it is common to use secondary radioactive isotopes (of lesser abundance) as reference isotopes once they have been positively identified, enabling more precise scaling to low yield, unstable isotopes.

Beam Dynamics

Individual target assemblies may differ due to design, fabrication, extraction voltage and output charge state. The IMS beamline optics are designed to accept extracted ion beams from either east or west target station (ITE/ITW) and render them suitable for separation by proper collimation and focussing before transmission to the rest of the ISAC facility.

Ion optics elements are considered in two separate categories - matching and transport. Matching quadrupoles and steerers are used to manipulate the focus and steering of the beam to meet design specifications. Transport sections are designed to accept matched beams and transmit them to an image point, after which either another transport section begins or beam can be further matched. Transport section quadrupoles are interdependent - the relationship between adjacent element voltages must remain constant. On the other hand, matching optics (while having theory values), can be tuned to correct for imperfections and asymmetries caused by the previously noted factors.

Ion Optics

Collimated ion beams emitted from sources have a natural tendency to diverge due to space charge effects and the intrinsic kinetic energy of each individual ion within the beam. While for low intensity beam currents (several nanoAmperes), space charge does not play a significant role, the latter effect does. Successful transport requires submitting the beam to periodic forces which will counteract these tendencies, in addition to matching beam properties to experimental requirements.

Similar to the optics of massless photons, the optics of nonzero mass ion beams in a vacuum involve the tracing of ion trajectories after interaction with lenses of various focal lengths, and drift spaces. Assuming a collimated beam extracted from a source with a discrete energy, the passage of charged particles through electric and magnetic fields is governed by the Lorentz force law:

$$\vec{F} = q(\vec{E} + \vec{v} \times \vec{B}) \tag{13}$$

For low energy beams, the use of electrostatics is more convenient due to the fact that magnetic forces are on the order of E/c, and thus require much more intense fields to produce a similar effect[5]. For simplicity, zeroth or first order forces are desired to act upon ion beams. These linear forces should be of the form:

---

[5] this situation reverses itself at medium and high energies where the generation of strong magnetic fields is easier due to the availability of high current low voltage power supplies, as opposed to the generation of extremely high electric fields.

$$E_{i0} = k, E_{i1} = kx_i \tag{14}$$

recalling that the electric field is the gradient of a scalar potential, which must satisfy Laplace's equation:

$$E = -\nabla V, \quad \nabla^2 V = 0 \tag{15}$$

Beam steering can be accomplished using a set of parallel plates across which a voltage potential is sustained. The resulting linear electric potential will generate a constant lateral electric force, which will displace the beam. To allow full transverse steering of the beam, sets of steerer plates are generally installed back to back within the beamline vacuum section. On the other hand, in order to accomplish linear focussing fields, the solution of Laplace's equation implies that a general focussing potential V_f of the form:

$$V_f = \frac{k}{2}(y^2 - x^2) \rightarrow F_{E_i} = -kx_i \tag{16}$$

must be used. Note the constraint imposed by the requirement of Laplace - the signs between (x,y) must be inverted. This means that for multipolar ion lenses, focussing in one dimension always implies defocussing in the other. Thus, in order to accomplish desired beam envelope manipulations, lenses which produce this type of field will always have to be used in n-tuplets, frequently doublets or triplets. The potential listed in Eq. 16 is known as a quadrupole, as it can be produced by using four charge sources, producing an electric field shown in Figure 8.

Another benefit of using quadrupole n-tuplets is the principle of alternate gradient focussing. Also known as strong focussing, this principle holds that a charged particle beam passing through alternating x and y electromagnetic focussing gradients will gradually achieve a higher net degree of focussing in both transverse dimensions.

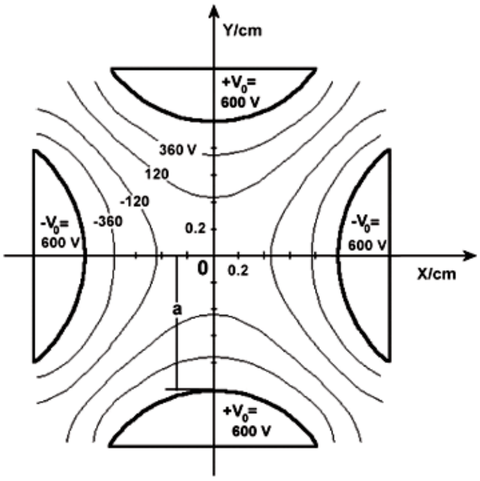

Figure 8: Quadrupole electric field generated by 4 opposed electrodes. The distance a denotes the aperture radius.

Quadrupoles are thus ion lenses whose focussing strength is linear to the voltage potential with which they are supplied. The focal length of a quadrupole lens can be expressed as:

$$\frac{1}{f} = \frac{V_Q}{V_0}\frac{L}{a^2} \tag{17}$$

where V_Q is the quadrupole voltage, V_0 is the beam voltage, L is the axial length of the electrodes and a is the aperture radius. Electrostatic quadrupoles at ISAC are designed with $a = 1''$. As an example, for a 30kV ion beam, quadrupole L = $2''$, $V_Q =$ 1kV, the focal length works out to approximately $15''$.

Quadrupole lenses not only focus, they can also steer, an effect which should be minimized at all costs. Looking at Eq. 16, an argument of symmetry can be made: firstly, the focussing effect is null for beam passing through the origin. For any arbitrary nonzero point (x_n, y_n), the deflecting electric forces will be $F_E = -kx_n, -ky_n$. Now, in the event of a symmetrically distributed beam centered at the origin, the electric forces will be identical but opposite for all beam components on either side of the origin, for both x and y, resulting in a steering free focus.

However, if beam flies through a quadrupole off-center, no longer symmetric about the origin, with a beam centroid of (x_0, y_0), the corresponding electric forces for any beam component at $(x + x_0, y + y_0)$ will become: $F_E = -kx - kx_0, -ky - ky_0$. This results in a set of constant offsets $(-kx_0,\ -ky_0)$, with the parameter k depending on the quadrupole voltage. Not only will beam exiting the quadrupole aperture be displaced proportionally to its entrance offset, but changing the quadrupole voltage will cause lateral displacement in both x and y, in effect steering the beam. Considering that quadrupoles generally come in pairs or triplets, it is obvious that such an effect will compound itself, producing a distorted beam profile far downstream and necessitating the use of even more steering throughout the tune to correct for this. Moreover, setting downstream quadrupole values to theory will not produce the expected beam properties.

Focussing can also be accomplished using a segmented unipotential lens, commonly known as an Einzel lens. This device consists of three consecutive, concentric, segmented tubes with the first and last at ground relative to beam voltage, and the center tube at some different potential V_e, as shown in Figure 9. Given both the Einzel lens' dependency on beam energy and the dynamics of its focussing mechanism, no closed form analytical expression exists for the focal length of an Einzel lens. Instead, these properties are simulated using ion-optics codes which approximate the solution using various numerical calculus methods. However, from a qualitative standpoint, the focussing mechanism works as follows: by holding the central electrode at either a negative or positive potential with respect to beam voltage, a valley is effectively created in the potential energy field permeating the central electrode region. This valley has an inherent saddle shape which is a consequence of the application and solution of Equation 15. Depending on the polarity of the central electrode, particles traversing it will either fall or climb into this potential energy valley, whose 2-dimensional projection has an inherent saddle shape, as shown in Figure 9. Particles exiting the central region then climb up or fall back to beam ground potential, with the shape of the potential surface causing a radially dependant *rolling in* effect, causing a focus. Note that an Einzel lens can be operated with the central electrode at negative or positive potential with respect to beam voltage. Operating an Einzel lens with a negative central electrode results in a much stronger focus.

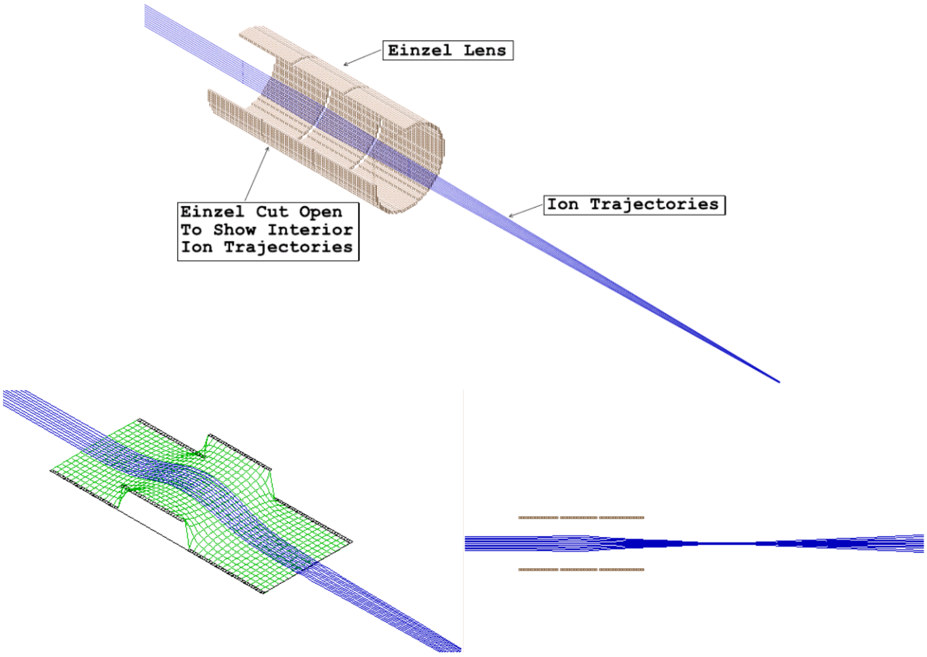

Figure 9: Top: cutaway view of a simulated Einzel lens, showing ion trajectories from top left to bottom right. Left: 2D projection of an Einzel lens (positive central electrode) equipotential energy surface, with ion trajectories (from top left to bottom right) crossing the lens. Observe how the shape of the potential surface causes a net focussing effect when exiting the lens. Right: 2D cross section of an Einzel lens (negative central electrode) showing the net focussing effect on a distribution of charged particles propagating from left to right. All of these are generated in SIMION, an ion optics simulation package.

Since the electrostatic potential in the lens is symmetric, it achieves focussing in both x and y simultaneously. However, the advantage of alternate gradient focussing is lost. Typically, an Einzel lens will be employed at the ion source front-end, allowing for a coarse adjustment of the ion beam focus prior to matching into the alternating gradient focussing provided by quadrupole n-tuplets.

While at a macroscopic level an ion beam can be considered as a product of its envelope, at the microscopic level it is composed of numerous charged particles. As any other statistical collection, there will be a distribution of positions and momenta, which will depend on the initial conditions at the target. Understanding the behavior of these distributions is critical to understanding exactly what can be done in terms of beam tuning with the above optics - whether or not certain features of the ion beam can be modified. To quantify this, something measurable must be provided which can track the effects of tuning on extracted beams.

Liouville's Theorem and Emittance

The concept of phase space is useful to map out the state of a system such as collections of particles. Concretely, the phase space is the space representing all physical coordinates that describe the ensemble. In the case of an ion beam, this cooresponds to $(x_i, p_{x_i}), i = 1, 2, 3$, the three dimensional position coordinates and their momenta in those same coordinates. The distribution function of a system of particles is a function of all phase space variables (6 in all), which gives the hypervolume of phase space density of a system. More simply, it gives the number of particles at a point (x, y, z) with momenta (p_x, p_y, p_z):

$$f(x_i, p_i) = f(x, p_x, y, p_y, z, p_z) \tag{18}$$

Liouville's theorem governs the time-evolution of phase space coordinate distributions. It is a statement about the relationship between the position and momentum of a system, and how both affect each other, as a consequence of conservation of momentum and energy. Succinctly, Liouville's theorem states that:

The distribution function is constant along any path in phase space. (19)

A path in phase space can simply be thought of as a consequence of motion. Liouville's theorem only applies in the presence of *conservative* forces, *i.e.*, forces for which the work done is path-independent[6]. Liouville's theorem implies that as particles move about in space with their respective momenta and undergo external forces [7], the exchange of momenta and positions from one coordinate to the next (x to y, y to z, etc..) cannot exceed the total available phase space volume that the system possesses. This is a direct consequence of conservation of energy and momentum. In light of this, Liouville's theorem can be thought of in simpler terms:

$$\boxed{\textit{The phase space volume of a system is conserved.}}$$

In the case of an ion beam, the initial phase space volume will be determined by the source extraction prameters such as voltage, temperature (which affects the kinetic energy of the ions), as well as the geometry of the electric fields present at the front-end. Thus, the design of ion sources must take into account the ion distributions that will be produced, for once beam exits the source it is no longer possible to change its phase space volume in a drift space

The Emittance of a beam is a measure of its phase space distribution, which is used to quantify its state. Strictly speaking, it is defined as the 6-dimensional integration over the phase space hypervolume defined by its density function:

$$\epsilon_6 = \int \cdots \int_{V_6} dx_i \, dp_i, i = 1, 2, 3 \tag{20}$$

The 6-dimensional total emittance ϵ_6 can be subdivided into the 2-dimensional longitudinal emittance ϵ_L and the 4-dimensional transverse emittance ϵ_T, which are generally uncoupled, given the approximate independence of transverse and longitudinal motion. At constant energy, which is the case for drift spaces such as the IMS section, the momenta can be removed from the integration:

$$\epsilon_T = \iiiint_{V_T} dx \, dp_x \, dy \, dp_y = \vec{p^2} \iiiint_{V_T} dx \, dx' \, dy \, dy', \tag{21}$$

---

[6] A static electric field satisfies this criterion.

[7] in this case, the Lorentz force caused by transit through the electric fields of steerer plates and quadrupoles

the substitution $x' = dx/dz$ follows from the fact that x' is the angle subtended by the axial and transverse motions v_z and v_x. Assuming the beam energy greatly exceeds the transverse energy, a small angle approximation produces:

$$tan(x') \sim x' = \frac{v_x}{v_z} \rightarrow dx' = \frac{dx}{dz} \tag{22}$$

This introduces the convenient concept of **trace space** in which the transverse emittance now only depends on the physical coordinates (x,x') and (y,y'), free of time or energy dependencies. Measuring the transverse emittance becomes a purely geometrical operation, requiring a measurement of position and angle. In a drift space where (x,y) coordinates are uncoupled, the transverse emittance can now be written as:

$$\epsilon_T = \iint dx\, dx' \cdot \iint dy\, dy' = \epsilon_x \cdot \epsilon_y; \tag{23}$$

measuring the transverse emittance then consists of sequentially measuring the horizontal and vertical emittances, and multiplying their products. In practice, the integration of Eq. 23 is accomplished by averaging a beam current with a Faraday cup over some defined time interval. This practical measurement is referred to as the root-mean-square (RMS) emittance, and is defined as:

$$\epsilon^2_{rms} = \langle x_i^2 \rangle \langle x_i'^2 \rangle - \langle x_i x_i' \rangle^2 \tag{24}$$

where $\langle .. \rangle$ denotes the averaging over the ensemble. In ISAC, this measurement is accomplished thanks to what is called the emittance rig, whose conceptual function is shown in Figure 10.

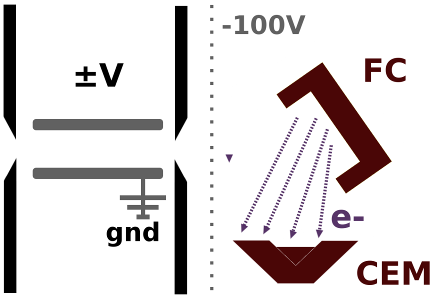

Figure 10: Schematic representation of the ISAC Emittance Rig (not to scale). Beam enters between the slits from left to right.

Instead of measuring the entire beam at once, it is broken into subsets known as a beamlets. These beamlets are defined with a set of slits, visible on the left hand side of Figure 10. The position measurement is accomplished by step-motor, moving the entirety of the rig laterally in small increments, while the angular measurement is accomplished by deflecting the beamlet with a variable voltage ±V. For high current situations, a Faraday cup (FC) located beyond the slits integrates the current. For low current situations, a perpendicularly mounted channeltron (CEM) measures secondary electrons emitted by ion collisions on the FC. A negatively-biased grid (dotted line) helps to define a local electric field which guides the electrons toward the CEM. To alternate between horizontal and vertical emittances, the rig is rotated 90° around the beam axis and the measurements repeated.

Typical low energy emittances generally take on the form of an ellipse with diffuse edges as the particle distribution does not have a clear cutoff, tailing off to infinity with asymptotically diminishing probabilities. This is practically circumvented by fitting the ellipse to some cutoff value, typically for 90% beam containment bounds [11]. The trace-space RMS emittance fit (Eq. 24) allows for the calculation of the ellipse area A_e or simply the half-axis product $E_{xx'}$, defined as:

$$A_e = \pi ab \tag{25}$$

$$E_{xx'} = \frac{A_e}{\pi} = ab \tag{26}$$

where a,b are the semiminor and semimajor axes of the ellipse. Eq. 25 is the true ellipse area, while Eq. 26 is known has the semi- or half-axis product[8]. Given the trace-space dimensions (x,x'), position and angle, both of these are expressed in units of position $\cdot$ radians, producing units of length (since radians are dimensionless). In the literature and the field, it is not uncommon to encounter $\pi mm \cdot mrad$ (milliradians), which is a notorious source of confusion in beam and accelerator physics. The use of $\pi mm \cdot mrad$ was historically intended to symbolize that π was factored out of the area (Eq. 25), however the gradual transition to using RMS emittance as a benchmark (Eq. 26) introduced the possibility to confuse both total area and semi-axis product.

The effect of a focussing ion lens can now be understood in terms of the emittance ellipse, and is shown in Figure 11 where a well matched beam is being focussed. The trace space ellipse is tilted at -45° in the lens, indicating a balance between the position spread and momentum distribution. As the beam begins converging towards the focal point, the position spread begins to decrease (horizontal axis). Simultaneously, given that the quadrupole field force is linearly proportional to distance from the central beam axis, particles further away experience a stronger acceleration than those closer to the origin (Eq. 16). This widens the momentum distribution, with extremal particles drifting towards the focal point at greater transverse velocity than those in the central beam region. At the focal point, the position spread is momentarily minimized as most ions, regardless of their velocity, happen to occupy a smaller volume of space with the emittance ellipse being vertical. After transit through the focal point, particles continue transverse drift at their respective velocities causing the ellipse to keep rotating. The snapshot ends with the ellipse rotated a full 90°. It is clear that, in the absence of further ion optics to keep focussing the beam downstream, it would simply drift apart due to its inherent momentum distribution.

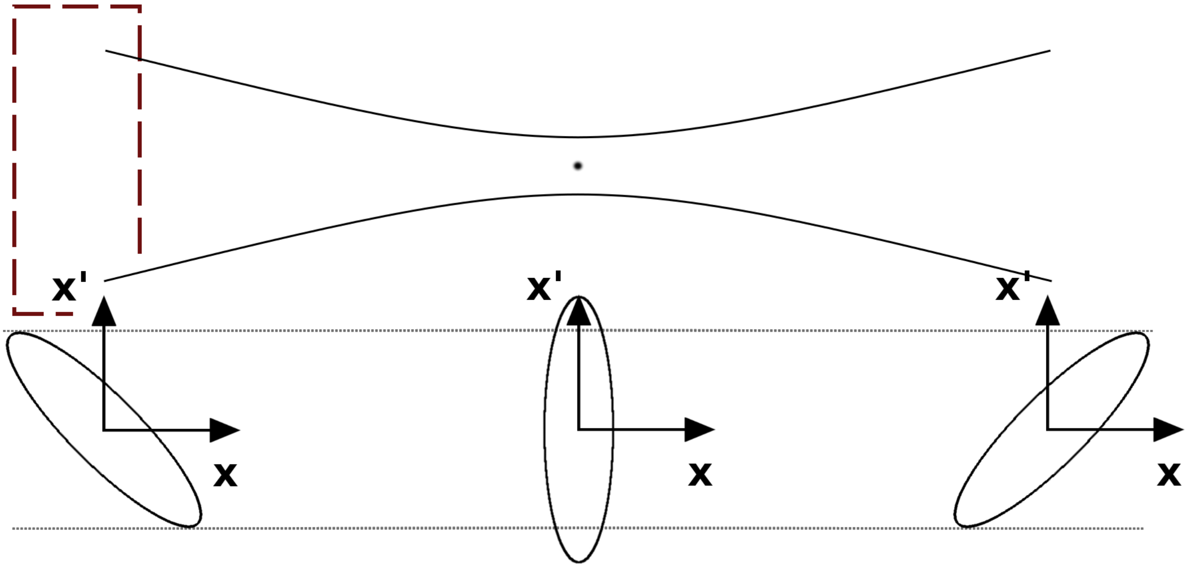

Figure 11: Sequential evolution of the transverse emittance area of an ion beam being focussed by a converging electrostatic lens (dotted red line). The emittance ellipses are shown on the bottom, corresponding to a snapshot of beam emittance above.

The above situation is a direct example of Liouville's theorem. Since the momentum distribution is inherent to the particles and is position-independent within the beam, it cannot be eliminated. A linear force will cause all particles to accelerate in a certain direction, but the initial spread in momenta will become a position spread. To do away with this, it would be necessary to give each individual particle a varying degree of acceleration to cause them all to drift at the same speed. This is thermodynamically impossible.

Separator Field Corrections

The transverse cross section of the separator magnet magnetic field can be expressed in cylindrical coordinates as:

$$B = B_0\Big[1 - \alpha\frac{r - r_0}{r_0} + \beta(\frac{r - r_0}{r_0})^2 + ...\Big] \tag{27}$$

where α and β are magnetic field indices. Both these parameters can be thought of as aberration parameters, which will produce first and second order distortions in the field $B(r)$. Such aberrations will have an effect on both horizontal and vertical emittance profiles. As beam optics are designed to accept beams with elliptical emittances, aberrations to the separator field can then

---

[8] since π is a constant, removing it from the value of emittance simplifies the expression. This is basically the equivalent of using the squared radius as a proxy to the total area of a circle - since this number is not multiplied by an irrational, it tends to make things simpler.

produce a degradation in transmission post-separator.

First order aberrations (α) will induce a change in magnetic focal length, in other words they will result in a displacement of the beam waist along the beam axis. On the other hand, second order (β) aberrations will cause parabolic warping of the trace-space emittance ellipse. Physically, α aberrations are the result of an incorrect magnetic field gradient, while β aberrations are the result of magnetic pole surface imperfections.

The 135° separator is designed with two sets of field correction coils, known as the α and β coils, in the form of printed circuit boards above and below the magnet as shown in Figure 12. The α coil produces a unidirectional current running the length of the separator magnet beam path, while the β coil is segmented into a forward and return current section running parallel to eachother. This produces a linear field correction for the α coil shown in the top right part of Figure 12 as the curve b, while the β coil produces a second order parabolic field adjustment shown on the bottom right hand side of Figure 12.

The progressive effect of both coils on a ^{27}Al beam at 40.8kV is shown in Figure 13, measured at the emittance rig in the diagnostic box beyond the separator. The α coil can be seen to cause a rotation of the horizontal transverse emittance ellipse, corresponding to a change in focal length of the magnet. By design, the separator magnet should image at the mass selection slits in diagnostics box 11 (DB11), set to 0.8mm when the separator is run at its M/ΔM = 2000 configuration. α coil optimization thus generally produces an appreciable effect on beam transmission post-separator.

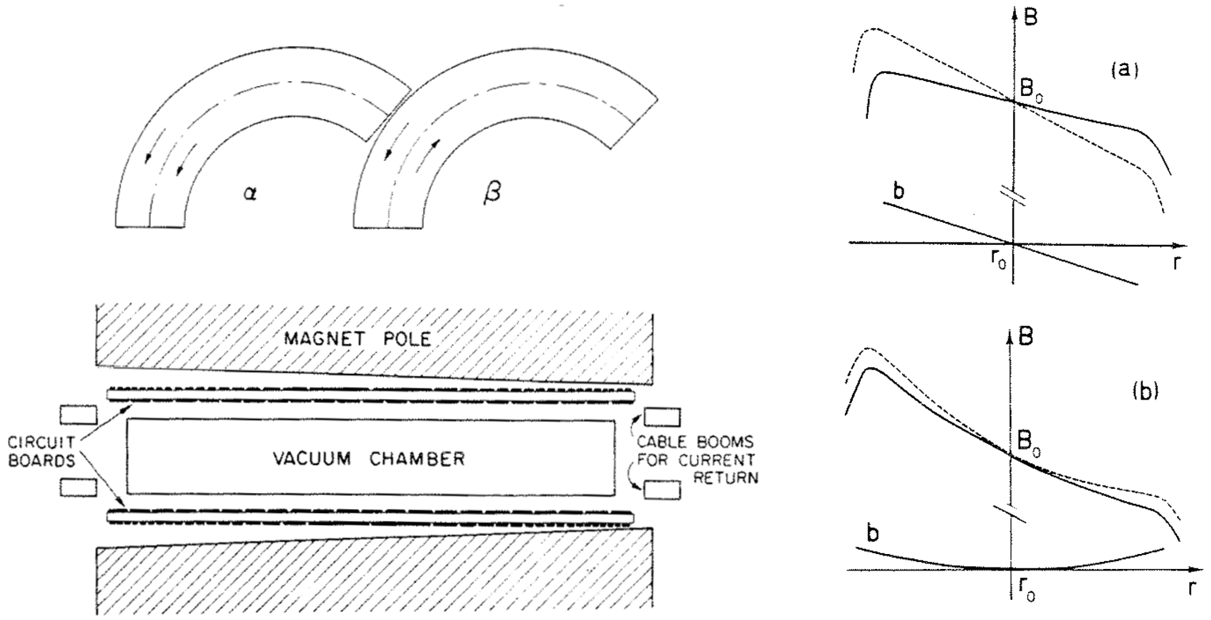

Figure 12: Bottom left: cross-section of the mass separator α and β coil printed circuit boards. The current return cables are located on separate cable booms located beside the vacuum chamber. Top left: representation of the current flow direction for α and β coils. Top right: typical effect of the α coil on the radial separator field profile. Bottom right: typical effect of the β coil on the radial separator field profile.

The β coil, with its parabolic correction, can be seen to cause (or eliminate) warping in the ellipse. The transport section imaging of a warped ellipse will introduce transmission and focussing problems as the beam propagates out of the IMS section, potentially resulting in preventable losses along the beamline, possibly causing unneeded radiation hot spots along the transport system. To counter this, during the initial setup of a target, transverse emittances are generally measured to determine target output performance and to ensure that both corrections are producing optimal emittances which translate into good beam transmissions. Also note that the α and β values are typically set on an abundant pilot isotope (due to ease of measurement on the emittance rig), then should be scaled with the isotope mass ratio.

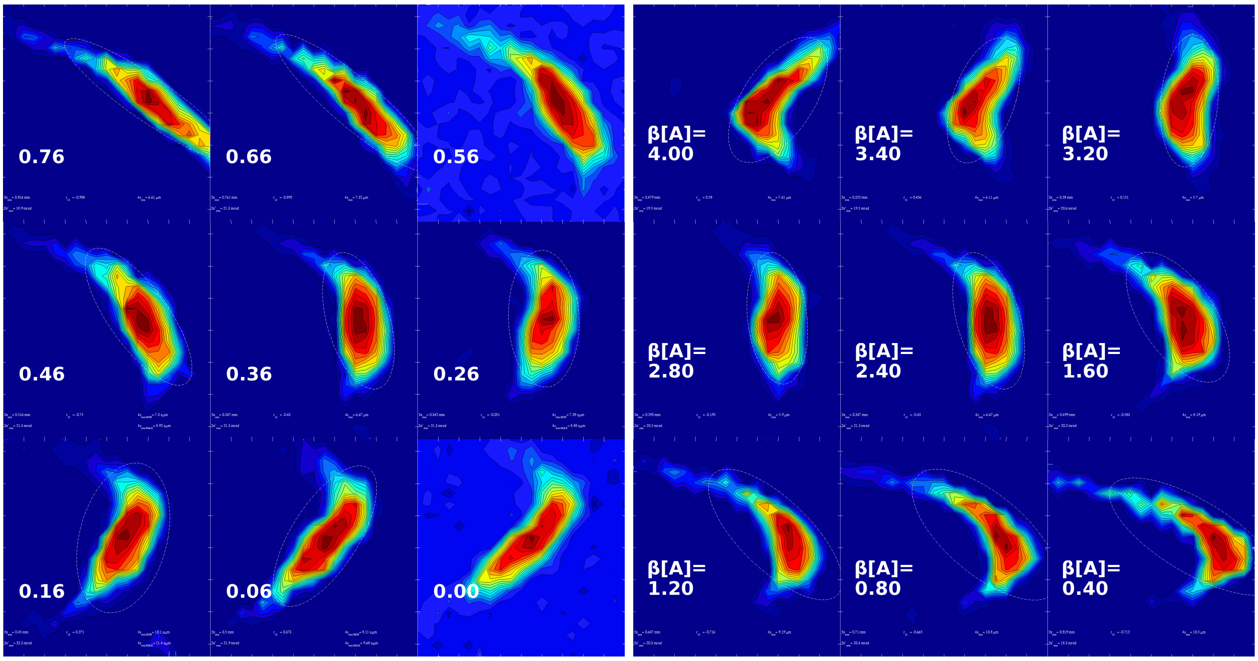

Figure 13: Left 3x3 tiles: Progressive effect of the alpha coil on horizontal emittance, starting at 0.76A (top left) to 0.00A (bottom right). Each frame corresponds to the coil being lowered by 0.1A. Right 3x3 tiles: Progressive effect of the beta coil, starting at 4A (top left) to 0.00A (bottom right). Each step corresponds to the coil being lowered by 0.4A. Taken with a 40.8kV ^{27}Al beam.

IMS Tuning Overview

The concepts covered to this point allow for a summary overview of the general considerations and technique that should govern setting up the IMS section, first on a pilot isotope, then on a potentially low yield radioisotope for experiment delivery.

Characterizing the output m/q distribution of a new target is one of the first things to be done in order to identify suitable pilot isotopes. This is usually achieved by performing what is known as a mass scan with the pre-separator magnet on the faraday cup immediately downstream. This involves scanning MB1's magnetic field across the range of expected masses that the target can produce. Bearing in mind the nuclear reactions at play, this usually means scanning from ^{7}Li to the mass of the target material. The exception to this procedure is when a target material is sufficiently well known to negate the need to hunt for pilot isotopes.

A pilot tune to the ISAC Yield Station is then established. Seeing as this tune out of the IMS section will form the basis for further tunes to experiments, particular care and attention should be given to ensure it is properly optimized and free of unnecessary optics variations. Beam exiting the target should be centered. Transport sections should be set to their theoretical values, matching sections tuned with minimal deviation from theory, and beam steering minimized to avoid *slaloming*, which reduces the associated nonlinearities.

Beam emittance is then examined with the emittance rig, producing more information about the performance of the target and quality of the tune. The target front-end is adjusted to produce good horizontal and vertical emittances. The Mass Separator α and β coils are fine-tuned to produce the best possible emittance profiles.

The measurement of isotope yields follows. Particular attention is generally given to isotopes that will be used in upcoming experiments, as well as isobaric contaminants that might affect data acquisition. This also brings up a critical safety issue. Target production mechanisms populate several isobars simultaneously, meaning that for a given A = N + Z value, it is likely that there will be several different radioisotopes present at this mass region. The stability of these isobars can vary significantly from one species to the next, translating in a wide range of half-lives. An excellent example of this is the A = 22 isobaric family, where all half-lives lie within a few ms to a few seconds, with the exception of ^{22}Na, with $t_{1/2} = 2.9$ years. Accidentaly delivery of this isotope will cause contamination that would take about 20 years to fall below 1% of its initial activity.

References

[1] Bricault, P.G., Dombsky, M.,
Rare isotope beams at ISAC - target & ion source systems
Hyperfine Interact. (2014) 225:25-49

[2] Bricault, P.G., Dombsky, M.,
High Power Target Developments at ISAC
Nucl. Instr. and Meth., 204 (2003) 319-324.

[3] Dombsky, M., Bricault, P.G., *et al.*
ISAC Target Operation With High Proton Currents
Nucl. Instr. and Meth., 204 (2003) 191-196

[4] Dombsky, M., Kunz, P.,
ISAC Targets
Springer Science (2013).

[5] Bricault, P.G., Dombsky, M., *et al.*
High Power Targets for ISOL Radioactive Ion Beam Facility
Proceedings of the 2003 Particle Accelerator Conference.

[6] Lavoie, J.P.,
Production of Pure Ion Beams by Laser Ionization and a Fast Release RFQ
Faculté des Sciences et de Génie, Université Laval, Québec (2010), p.10

[7] Uberuaga, B., Smith, R. *et al.*
Dynamical simulations of radiation damage and defect mobility in MgO
Phys. Rev. B, 71.104102 (2005).

[8] Russell, G.J,
Spallation Physics - An Overview
ICANS-XI International Collaboration on Advanced Neutron Sources (1990)

[9] Lynch, W.G.,
Nuclear Fragmentation In Proton And Heavy-Ion-Induced Reactions
Ann. Rev. Nucl. Part. Sci. (1987) 37:493-535

[10] Bricault, P., Baartman, R., *et al.*,
TRIUMF-ISAC Target Station and Mass Separator Commissioning
Elsevier Preprint, 30 March (2000).

[11] Stockli, M.P.,
Measuring and Analyzing the Transverse Emittance of Charged Particle Beams
American Institute of Physics (2006) 978-0-7354-0369-7/06